Jordanian Journal of Computers and Information Technology (JJCIT), Vol. 12, No. 04, December 2026.

EFFECTIVE CAPACITY OF ARR-AIDED NOMA NETWORKS UNDER PHASE MISALIGNMENT AND IMPERFECT SIC

Chi-Bao Le[1] and Tin Phu Tran[2]

(Received: 28-Aug.-2026, Revised: 20-Oct.-2026 and 24-Oct.-2026, Accepted: 26-Oct.-2026)

ABSTRACT

The presented work explores the combined effect of non-ideal successive interference cancellation (SIC) and phase errors on the effective capacity (EC) of NOMA networks with the assistance of active reconfigurable repeaters (ARRs). To study the system behavior with strong restrictions on delay requirements, the Gauss-Chebyshev quadrature technique is employed to develop accurate approximate formulae for the EC of near and far users over independent Rayleigh fading channels. Moreover, detailed asymptotic analysis is performed in high and low SNR regimes to obtain physical insights. The analytical and numerical results indicate the existence of fundamental limits in system performance: in the high SNR regime, the EC of the NOMA users is limited by deterministic error floors determined only by the power allocation parameters and residual interference and is entirely independent of channel characteristics and delay requirements. Conversely, in the low-SNR power-limited regime, the effective capacities scale linearly with the transmit SNR. In addition, the results indicate that strict quality-of-service (QoS) requirements and large phase errors severely limit transmission rates. However, even in the presence of imperfections in the hardware and channel, the suggested ARR-based NOMA architecture significantly outperforms the conventional OMA architecture in the low-to-medium SNR regime.

KEYWORDS

Effective capacity, Non-orthogonal multiple access (NOMA), Active reconfigurable repeater (ARR), Imperfect successive interference cancellation (SIC), Phase misalignment error, Delay constraints.

1. INTRODUCTION

The shift toward the beyond fifth-generation (B5G) and sixth-generation (6G) wireless eras brings a paradigm shift in how we handle global data traffic. We are no longer just looking at the need for higher data rates; ultrareliable and low-latency communications (URLLC) have become strictly mandatory for emerging applications, like autonomous driving, industrial automation and augmented reality [1]-[4]. To address these stringent latency and reliability requirements, emerging physical-layer technologies operating under strict low-latency communication constraints have been actively investigated for B5G/6G systems [4]. To handle this explosive demand without exhausting the severely limited radio spectrum, non-orthogonal multiple access (NOMA) has taken center stage [5]-[6]. Unlike conventional orthogonal multiple access (OMA) setups that rigidly assign distinct time or frequency slots to individual users, NOMA boldly serves multiple users within the exact same resource block [7]. It achieves this by multiplexing signals in the power domain, which radically boosts spectral efficiency while ensuring fairness among users with diverse channel conditions. However, these advanced network architectures frequently encounter severe electromagnetic wave propagation hurdles. In dense urban environments, direct communication links between the base station and end-users are easily severed by physical blockages, like tall buildings or moving vehicles, inevitably leading to devastating signal attenuation and dead zones [8].

As a remedy to these coverage holes, researchers have heavily investigated the integration of cooperative relaying into NOMA networks [9]-[10]. While passive reconfigurable intelligent surfaces (RISs) initially caught the eyes of the research community due to their near-zero power consumption, they fundamentally suffer from a severe "double path-loss" penalty, which drastically limits their practical coverage area [11]. To bypass this critical limitation, active reconfigurable repeaters (ARRs) have recently emerged as a highly compelling alternative [12]. Equipped with active amplification

1. C.-B. Le (Corresponding Author) is with the Faculty of Information Technology, Ton Duc Thang University, Ho Chi Minh City, Vietnam. Email: lechibao@tdtu.edu.vn.
2. P. T. Tran is with the Natural Language Processing and Knowledge Discovery Research Group, Faculty of Information Technology, Ton Duc Thang University, Ho Chi Minh City, Vietnam. Email: phutrantin@tdtu.edu.vn.

components, ARRs do not merely reflect incident waves in a passive manner. Instead, they actively steer and boost the superimposed NOMA signals before forwarding them to the intended users [13]. This active forwarding mechanism effectively mitigates the multiplicative fading effect, offering a much stronger and reliable signal at the receiver end [14]. Despite their undeniable physical advantage, deploying ARRs in real-world scenarios introduces a new set of hardware challenges. A practical ARR implementation typically relies on highly directive sectorized antennas to focus its transmission beams [15]. Consequently, a fundamental vulnerability arises: the overall system performance becomes highly sensitive to phase misalignment [16]. Due to unavoidable beam-tracking deviations, unpredictable user mobility and quantization errors, the actual physical angle of the receiving user rarely matches the repeater's intended beam direction perfectly. When such misalignment occurs, the transmitted signal inevitably spills over into the side-lobes. This signal leakage drastically degrades the main-lobe gain and essentially cripples the reliability of the entire transmission link. On the receiver side, the fundamental success of the NOMA protocol hinges entirely on the successive interference cancellation (SIC) mechanism [17]. In purely theoretical studies, perfect SIC is often taken for granted. Yet, scanning the technical literature reveals that achieving ideal SIC in practice is a heavily flawed assumption [18]. Hardware non-linearities, imperfect channel estimation, residual in-phase and quadrature imbalance (IQI) [19] and error propagation make residual interference an unavoidable reality [20]. This imperfect SIC directly penalizes the near user, as the leftover interference from the far user's signal severely restricts the near user's decoding capability and limits the maximum achievable throughput [21]. Beyond these physical layer impairments, assessing the true potential of these networks requires an appropriate performance metric. Traditional Shannon capacity models assume infinite block lengths and unlimited buffering, making it a rather poor choice for analyzing delay-sensitive B5G/6G applications [22]. To accurately capture the system's ability to handle strict quality of service (QoS) requirements, effective capacity (EC) must be utilized [23]. As a cross-layer metric, EC mathematically quantifies the maximum constant data arrival rate that a wireless channel can reliably support while strictly adhering to a predefined delay exponent [24]. Main-lobe gain essentially cripples the reliability of the entire transmission link.

Table 1. Comparison of the proposed work with existing literature.

Ref.	Access Scheme	Assisting Device	Phase Errors	High/Low SNR	SIC Status	Key Evaluated Metrics
[13]	NOMA	ARR	✓	✓	Ideal	Outage Probability and Ergodic Capacity
[14]	RSMA	Repeater	×	×	Ideal	Outage Probability and Ergodic Rate
[15]	OMA	Repeater	×	×	N/A	N/A
[16]	OMA	Repeater	×	×	N/A	Capacity
[32]	NOMA	Repeater	×	×	Ideal	Bit Error Rate and Secrecy Outage Probability
[33]	NOMA	RIS	×	✓	Residual	Secrecy Outage Probability
[34]	NOMA	Holographic	×	×	Ideal	Average Block Error Rate
[35]	NOMA	Holographic	✓	✓	Ideal	Outage Probability
Proposed	NOMA	ARR	✓	✓	Residual	Effective Capacity (Delay-constrained)

On the receiver side, the fundamental success of the NOMA protocol hinges entirely on the successive interference cancellation (SIC) mechanism [17]. In purely theoretical studies, perfect SIC is often taken for granted. Yet, scanning the technical literature reveals that achieving ideal SIC in practice is a heavily flawed assumption [18]. Hardware non-linearities, imperfect channel estimation, residual in-phase and quadrature imbalance (IQI) [19] and error propagation make residual interference an unavoidable reality [20]. This imperfect SIC directly penalizes the near user, as the leftover interference from the far user's signal severely restricts the near user's decoding capability and limits the maximum achievable throughput [21]. Beyond these physical layer impairments, assessing the true potential of these networks requires an appropriate performance metric. Traditional Shannon capacity models assume infinite block lengths and unlimited buffering, making it a rather poor choice for analyzing delay-sensitive B5G/6G applications [22]. To accurately capture the system's ability to handle strict quality of service (QoS) requirements, effective capacity (EC) must be utilized [23]. As a cross-layer metric, EC mathematically

quantifies the maximum constant data arrival rate that a wireless channel can reliably support while strictly adhering to a predefined delay exponent [24].

In recent years, to address the stringent spectral efficiency, latency and coverage expansion demands of B5G and 6G networks, various advanced cooperative multiple access, fluid antenna and reconfigurable relaying paradigms have been extensively explored in the literature. For instance, the performance of cooperative NOMA networks assisted by multi-antenna relays under hardware non-idealities was examined in [25], while the impact of keyhole fading channels and imperfect SIC on multi-access transmission was theoretically analyzed in [26]. To improve energy efficiency in green Internet of Things (IoT) deployments, ambient backscatter-assisted passive relaying with energy harvesting was proposed in [27]. Furthermore, active reconfigurable intelligent surfaces (RISs) have been integrated into IoT and satellite-terrestrial relay networks to enhance physical-layer security and multi-cast transmission reliability [28]-[29]. In ultra-dense and spatial diversity architectures, dynamic power control strategies for cell-edge NOMA users were studied in [30], transmit power optimization in unmanned aerial vehicle (UAV)-integrated IRS systems was investigated in [31] and the block error rate of fluid antenna systems under short-packet constraints was evaluated in [4]. Despite these significant advancements across relaying, fluid antenna, backscatter and RIS-assisted NOMA networks, the joint impact of active reconfigurable repeaters (ARRs), phase misalignment errors and imperfect SIC on cross-layer effective capacity remains unaddressed.

To strictly delineate our technical advances over closely related prior literature, particularly [13], it is essential to clarify the model inheritance and novel contributions. Specifically, our work inherits from [13] the foundational dual-hop ARR propagation architecture over Rayleigh fading, the sectorized antenna amplitude response under phase tracking error statistics $\left(\tau_i^2 \in \{\mu_i, \nu_i\}\right)$ and the modified Bessel PDF of cascaded Rayleigh fading channels. However, [13] was strictly restricted to traditional physical-layer metrics (outage probability and ergodic capacity) under the ideal assumption of infinite delay tolerance and perfect SIC. In sharp contrast, this paper substantially extends [13] to a cross-layer delay-constrained paradigm under imperfect SIC (κ). To the best of the authors' knowledge, a rigorous analytical framework that jointly evaluates the effective capacity of ARR-assisted NOMA systems under the combined threats of phase misalignment and imperfect SIC is noticeably absent from the current literature. Furthermore, our asymptotic analysis uncovers a vital engineering insight absent in [13]: while strict delay requirements (ϑ) severely penalize throughput in low-to-medium SNR regimes, the high-SNR capacity floor is dictated strictly by power allocation (a_1, a_2) and residual interference (κ), remaining completely immune to delay exponents and phase alignment statistics. Motivated by this critical gap, this work aims to provide a comprehensive performance assessment of such networks operating over independent Rayleigh fading channels. To clearly illustrate how our study advances the state-of-the-art, Table 1 visually summarizes the differences between our proposed framework and closely related works, highlighting the unique metrics and practical conditions evaluated in our research.

Against this background, the primary technical contributions of this paper are articulated as follows:

- We inherit the ARR sectorized antenna gain model and cascaded Rayleigh channel PDF from [13] and extend the system model to incorporate practical imperfect SIC (κ), formulating a comprehensive SINR model under joint phase misalignment and residual interference.
- We derive accurate, computationally efficient closed-form expressions for the EC of both the near and far users, leveraging the Gauss-Chebyshev Quadrature (GCQ) method to resolve the complex integral structures associated with cascaded fading channels.
- We conduct a rigorous asymptotic analysis in the high-SNR and low-SNR regimes. Our derivations mathematically prove that inter-user and residual interference lead to strict capacity ceilings at high SNRs, while the capacities scale linearly in the power-limited region.
- We provide extensive Monte Carlo simulations to validate the exactness of our theoretical derivations. The numerical findings offer deep insights into the fundamental capacity trade-offs between NOMA users, the critical penalties imposed by stricter delay constraints and the performance superiority of NOMA over OMA in low-to-medium SNR regions.

The rest of this paper is organized in the following manner. Section 2 outlines the theoretical framework of the proposed system model. Following this, Section 3 is dedicated to the detailed analytical

derivations for the performance assessment. The theoretical findings are then corroborated through comprehensive numerical simulations in Section 4, before bringing the study to a close with final remarks in Section 5. In summary, as visually highlighted in Table 1, the key novelty of this work lies in establishing the first analytical framework that jointly quantifies the effective capacity of ARR-assisted NOMA networks under the combined practical threats of phase misalignment and imperfect SIC.

Notation: Throughout this paper, a circularly symmetric complex Gaussian random variable with zero mean and variance σ^2 is represented by $\mathcal{CN}(0, \sigma^2)$. The statistical expectation and the probability of an occurrence are denoted by $\mathbb{E}(\cdot)$ and $\Pr(\cdot)$, respectively. Furthermore, the standard error function is given as $\mathrm{erf}(x)$, while $K_0(x)$ stands for the modified Bessel function of the second kind with order zero.

2. System Model

2.1 System Architecture

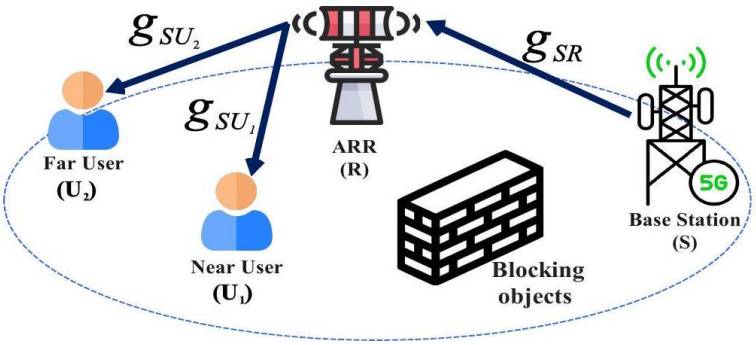


Figure 1. System model of the downlink ARR-assisted NOMA communication network.

As illustrated in Figure 1, we consider a downlink non-orthogonal multiple access (NOMA) communication system assisted by an active reconfigurable repeater (ARR). The network comprises a base station (S), an ARR node (R) and two NOMA users: a near user (U_1) and a far user (U_2). In practical complex environments, direct communication links between the base station and the end users are often severed by physical obstructions (e.g., tall buildings or other blocking objects). Consequently, the base station must rely entirely on the intermediate ARR to effectively forward the superimposed NOMA signals to both users. Let g_{SR} denote the channel coefficient for the link from S to R. Similarly, g_{RU_1} and g_{RU_2} represent the effective channel links from the repeater to U_1 and U_2, respectively. For the sake of analytical tractability and practical implementation, we assume that all nodes are equipped with a single antenna. Furthermore, perfect channel state information (CSI) is assumed to be available at the transmitting nodes [36]. This is a reasonable assumption in practice, as it can be achieved through reliable pilot-based channel estimation techniques operating under quasi-static fading conditions.

2.2 Channel Characteristics and Signal Transmission

To characterize the propagation environment, we assume that all underlying wireless links experience independent Rayleigh fading. Let g_{XY} denote the channel coefficient between a transmitting node $X \in \{S, R\}$ and a receiving node $Y \in \{R, U_1, U_2\}$. Consequently, the channel gain $|g_{XY}|^2$ inherently follows an exponential distribution. The probability density function (PDF) and the cumulative distribution function (CDF) of $|g_{XY}|^2$ are respectively formulated as [37].

$$f_{|g_{XY}|^2}(x) = \frac{1}{\Omega_{XY}} \exp\left(-\frac{x}{\Omega_{XY}}\right), \tag{1}$$

$$F_{|g_{XY}|^2}(x) = 1 - \exp\left(-\frac{x}{\Omega_{XY}}\right), \tag{2}$$

where $\Omega_{XY} = \mathbb{E}[|g_{XY}|^2]$ represents the average channel gain of the respective link, with $\mathbb{E}[\cdot]$ denoting the statistical expectation operator.

In accordance with the fundamental NOMA protocol [38], the base station linearly superimposes the

messages intended for the two users. The multiplexed signal broadcast by S is given by $x_s = \sqrt{a_1 P_s} s_1 + \sqrt{a_2 P_s} s_2$, where P_s is the total transmission power budget. Here, s_i denotes the normalized information symbol ($\mathbb{E}[|s_i|^2] = 1$) intended for user $U_i (i \in \{1,2\})$. To guarantee user fairness and facilitate successful Successive Interference Cancellation (SIC) at the near user, the power allocation factors are strictly ordered as $a_1 < a_2$, subject to the constraint $a_1 + a_2 = 1$.

The superimposed signal travels through the $S \rightarrow R$ link, gets processed by the ARR and is subsequently forwarded to the end users. The received signal at user U_i can be mathematically modeled as:

$$y_i = g_{SR} g_{RU_i} \theta_i \left(\sqrt{a_1 P_s} s_1 + \sqrt{a_2 P_s} s_2 \right) + n_i, \tag{3}$$

where $n_i \sim \mathcal{CN}(0, \sigma^2)$ denotes the additive white Gaussian noise (AWGN) at the receiver with noise variance σ^2 and θ_i defines the complex steering coefficient applied by the ARR towards U_i.

2.3 ARR Sector Antenna Model and Phase Misalignment

To actively direct its transmission, the ARR utilizes a beamforming technique. Mathematically, the complex steering coefficient θ_i is formulated in polar coordinates as $\theta_i = \tau_i \exp(j\varphi_i)$ [39]. Here, φ_i signifies the phase adjustment at the repeater, while $\tau_i \triangleq \tau(\phi_i, \tilde{\phi}_i) > 0$ specifies the amplitude response. The parameters ϕ_i and $\tilde{\phi}_i$ correspond to the intended beam direction from R to U_i and the actual physical angle between R and U_i, respectively [13]. Depending on the magnitude of the amplitude, the ARR functions as an active node if $\tau_i > 1$ and as a passive reflector otherwise. In this study, following the established ARR analytical frameworks in [13], [39], we adopt an idealized gain-only active repeater model. Specifically, the repeater is assumed to operate in a low-power active directional beam-shaping mode where the thermal noise added or amplified at the ARR is negligible relative to the destination receiver noise n_i. While practical high-power active relays introduce amplifier noise and strict power constraints, this idealized model maintains mathematical tractability for cross-layer effective capacity analysis while accurately capturing the primary beam-steering and gain characteristics.

Assuming a practical sectorized antenna pattern for the repeater, the amplitude gain τ_i behaves as a step function governed by the alignment accuracy [13]:

$$\tau_i = \begin{cases} \sqrt{\mu_i}, \text{ if } |\varepsilon_i| \leq \Theta_i, \\ \sqrt{v_i}, \text{ otherwise}. \end{cases} \tag{4}$$

In this specific model, the constant parameters $\mu_i > 0$ and $v_i > 0$ capture the primary lobe active gain and the side-lobe leakage of the ARR's radiation pattern, respectively. Moreover, Θ_i stands for the half-power beamwidth of the targeted beam. The discrepancy term $\varepsilon_i = \tilde{\phi}_i - \phi_i$ aggregates various system imperfections, such as quantization and beam-tracking deviations. According to [40], this misalignment variable ε_i is statistically modeled following a zero-mean Gaussian distribution, the standard deviation of which is configured as $\zeta_i = \sqrt{\Theta_i / 10}$. Consequently, the CDF for the tracking error ε_i is analytically derived as:

$$F_{\varepsilon_i}(x) = \frac{1}{2} \left(1 + \operatorname{erf} \left(\frac{x}{\sqrt{2\zeta_i^2}} \right) \right), \tag{5}$$

with $\operatorname{erf}(x)$ identifying the standard error function.

2.4 SINR Analysis under Imperfect SIC

At the receiver side, NOMA users apply the SIC mechanism to separate their desired signals from the non-orthogonal mixture. Following the decoding order based on channel qualities, the near user (U_1) first decodes the far user's signal (s_2) before subtracting it to retrieve its own message (s_1).

The signal-to-interference-plus-noise ratio (SINR) for U_1 to detect s_2 is expressed as:

$$\Gamma_{U_1 \to s_2} = \frac{a_2 \bar{\gamma} |g_{SR}|^2 \left|g_{RU_1}\right|^2 \tau_1^2}{a_1 \bar{\gamma} |g_{SR}|^2 \left|g_{RU_1}\right|^2 \tau_1^2 + 1}, \tag{6}$$

where $\bar{\gamma} = P_s/\sigma^2$ defines the average transmit signal-to-noise ratio (SNR). Assuming s_2 is successfully decoded, U_1 proceeds to decode s_1. However, due to hardware limitations and estimation errors, perfect SIC is rarely achieved [41]. Taking the residual interference into account, the effective SINR for U_1 to decode its own signal is given by:

$$\Gamma_{U_1 \to s_1} = \frac{a_1 \bar{\gamma} |g_{SR}|^2 \left|g_{RU_1}\right|^2 \tau_1^2}{\kappa a_2 \bar{\gamma} |g_{SR}|^2 \left|g_{RU_1}\right|^2 \tau_1^2 + 1}, \tag{7}$$

where $\kappa \in [0,1]$ parameterizes the severity of the imperfect SIC. Note that $\kappa = 0$ indicates the ideal perfect SIC scenario. In practical wireless transceivers, a non-zero κ typically originates from physical hardware non-idealities (such as power amplifier non-linearities, phase noise and IQ imbalance) as well as residual channel estimation errors during signal demodulation.

On the other hand, the far user (U_2) treats the signal of U_1 as interference and directly decodes its designated message s_2. The corresponding SINR at U_2 is formulated as:

$$\Gamma_{U_2 \to s_2} = \frac{a_2 \bar{\gamma} |g_{SR}|^2 \left|g_{RU_2}\right|^2 \tau_2^2}{a_1 \bar{\gamma} |g_{SR}|^2 \left|g_{RU_2}\right|^2 \tau_2^2 + 1}. \tag{8}$$

Remark 1: While this work focuses on a single-antenna setup to provide a tractable fundamental framework, extending the system to a multi-antenna architecture employing transmit antenna selection (TAS) with N_T antennas transforms the effective cascaded channel gain into a maximum order statistic $Z_{i,\,\mathrm{sel}} = \max_{1 \le j \le N_T} Z_{i,j}$. The resulting CDF becomes $F_{Z_{i,\,\mathrm{sel}}}(z) = \left[F_{Z_i}(z)\right]^{N_T}$. Under strict delay requirements (ϑ), deep fading events severely penalize the cross-layer effective capacity. TAS mitigates these deep fades by providing spatial diversity gain, which shifts the low-to-medium SNR effective capacity curves upward. However, in the high-SNR regime ($\bar{\gamma} \to \infty$), residual interference caused by imperfect SIC (κ) and power allocation (a_1, a_2) remains the dominant performance bottleneck. Consequently, the high-SNR capacity floor $R_{U_1}^{\infty} = \log_2\left(1 + \frac{a_1}{\kappa a_2}\right)$ is immune to spatial diversity, proving that multi-antenna selection enhances low-SNR power efficiency, but cannot bypass the high-SNR interference floor.

3. Effective Capacity Analysis

In this section, we evaluate the system performance under strict delay constraints by characterizing the EC [42]. Unlike traditional Shannon capacity, EC quantifies the maximum constant arrival rate that a wireless system can sustain while satisfying a predefined quality of service (QoS) requirement [43]. Mathematically, the EC for a given user i is defined as:

$$R_i(\bar{\gamma}, \vartheta) = -\frac{1}{Q} \log_2\left(\mathbb{E}\{(1 + \Gamma_i)^{-Q}\}\right), \tag{9}$$

where $Q = \frac{\vartheta TB}{\ln 2}$. Here, B represents the system bandwidth, T is the block duration and $\vartheta > 0$ denotes the QoS exponent which reflects the strictness of the delay constraint [42]. A larger ϑ implies a more stringent delay requirement.

3.1 Statistical Properties of the Misalignment Error

Before deriving the analytical EC for each NOMA user, it is necessary to address the statistical nature of the piece-wise amplitude response τ_i defined in (4). The distribution relies on the probability of the user being successfully aligned within the main lobe *versus* falling into the side lobe.

Using the CDF of the tracking error ε_i provided in (5), we can calculate the probability of successful beam alignment for user U_i. By expanding the probability inequality and applying the odd function property of the error function (i.e., $\mathrm{erf}(-x) = -\mathrm{erf}(x)$), the detailed mathematical steps are formulated

as:

$$\begin{aligned}\Pr(|\varepsilon_i| \le \Theta_i) &= \Pr(-\Theta_i \le \varepsilon_i \le \Theta_i)\\ &= F_{\varepsilon_i}(\Theta_i) - F_{\varepsilon_i}(-\Theta_i)\\ &= \frac{1}{2}\left[1 + \operatorname{erf}\left(\frac{\Theta_i}{\sqrt{2\zeta_i^2}}\right)\right] - \frac{1}{2}\left[1 + \operatorname{erf}\left(\frac{-\Theta_i}{\sqrt{2\zeta_i^2}}\right)\right]\\ &= \frac{1}{2}[1 + \operatorname{erf}(\rho_i)] - \frac{1}{2}[1 - \operatorname{erf}(\rho_i)]\\ &= \operatorname{erf}(\rho_i), \end{aligned} \tag{10}$$

where $\rho_i = \frac{\Theta_i}{\sqrt{2\zeta_i^2}}$. Consequently, the mutually exclusive probability of misalignment is strictly obtained as $1 - \operatorname{erf}(\rho_i)$.

Based on these mutually exclusive events, we denote $Z_i = |g_{SR}|^2 \left|g_{RU_i}\right|^2$ as the cascaded fading channel gain. Furthermore, let $H_i = Z_i \tau_i^2$ represent the overall effective channel gain. The PDF of H_i is calculated by splitting it into two parts [13].

$$f_{H_i}(x) = \operatorname{erf}(\rho_i) f_{\mu_i Z_i}(x) + [1 - \operatorname{erf}(\rho_i)] f_{v_i Z_i}(x). \tag{11}$$

3.2 Effective Capacity of the Near User (U_1)

For the near user U_1, the effective SINR after performing imperfect SIC is given by $\Gamma_{U_1 \to s_1}$ in (7). Substituting (7) and (11) into (9), the EC of U_1 is formulated as:

$$R_{U_1} = -\frac{1}{Q}\log_2\left(\operatorname{erf}(\rho_1)\mathcal{I}_{U_1}(\mu_1) + [1 - \operatorname{erf}(\rho_1)]\mathcal{I}_{U_1}(v_1)\right), \tag{12}$$

where the integral function $\mathcal{I}_{U_1}(x)$ encapsulates the expectation with respect to the cascaded channel Z_1 for a given amplitude gain $x \in \{\mu_1, v_1\}$:

$$\mathcal{I}_{U_1}(x) = \mathbb{E}_{Z_1}\left\{\left(1 + \frac{a_1 \bar{\gamma} Z_1 x}{\kappa a_2 \bar{\gamma} Z_1 x + 1}\right)^{-Q}\right\}. \tag{13}$$

3.3 Effective Capacity of the Far User (U_2)

Following a similar procedure for the far user U_2, the signal from U_1 is treated as interference. The EC of U_2 can be expressed by applying the SINR from (8) into the fundamental definition (9):

$$R_{U_2} = -\frac{1}{Q}\log_2\left(\operatorname{erf}(\rho_2)\mathcal{I}_{U_2}(\mu_2) + [1 - \operatorname{erf}(\rho_2)]\mathcal{I}_{U_2}(v_2)\right), \tag{14}$$

with the corresponding integral term given by:

$$\mathcal{I}_{U_2}(y) = \mathbb{E}_{Z_2}\left\{\left(1 + \frac{a_2 \bar{\gamma} Z_2 y}{a_1 \bar{\gamma} Z_2 y + 1}\right)^{-Q}\right\}, \tag{15}$$

where $y \in \{\mu_2, v_2\}$ represents the discrete gain states for U_2.

3.4 Analytical Evaluation *via* Gauss-Chebyshev Quadrature

To analytically evaluate the EC, the mathematical structures of the integrals $\mathcal{I}_{U_1}(x)$ and $\mathcal{I}_{U_2}(y)$ established in (13) and (15) must be thoroughly resolved. Notice that the random variables Z_1 and Z_2 are defined as the product of two independent, exponentially distributed variables (i.e., $Z_i = |g_{SR}|^2 \left|g_{RU_i}\right|^2$). Based on the statistical properties of cascaded Rayleigh fading channels, the PDF of Z_i is formulated as [44, Eq. (21)]:

$$f_{Z_i}(z) = \frac{2}{\Omega_i} K_0\left(2\sqrt{\frac{z}{\Omega_i}}\right), \tag{16}$$

where $\Omega_i = \Omega_{SR}\Omega_{RU_i}$ and $K_0(\cdot)$ denotes the zeroth-order modified Bessel function of the second kind.

By substituting (16) into the expectation in (13), the integral for U_1 is explicitly expressed over the semi-infinite domain $[0,\infty)$ as:

$$\mathcal{I}_{U_1}(x) = \int_0^{\infty} \underbrace{\left(1+\frac{a_1\bar{\gamma}zx}{\kappa a_2\bar{\gamma}zx+1}\right)^{-Q}\frac{2}{\Omega_1}K_0\left(2\sqrt{\frac{z}{\Omega_1}}\right)}_{\triangleq\mathcal{F}_{U_1}(z,x)}dz. \tag{17}$$

Due to the presence of the Bessel function multiplied by a fractional rational expression raised to a non-integer power Q, finding a direct exact closed-form solution using standard integral tables is mathematically intractable. To bypass this analytical hurdle without sacrificing accuracy, we deploy the Gauss-Chebyshev Quadrature (GCQ) method [45].

Specifically, we utilize the integral transformation provided in [45] to map the semi-infinite interval $[0,\infty)$ into the standard GCQ domain $[-1,1]$. By applying the variable substitution $u = \frac{4}{\pi}\arctan(z) - 1$, which yields $z = \tan\left((u+1)\frac{\pi}{4}\right)$, the differential element is derived as $dz = \frac{\pi}{4}\sec^2\left((u+1)\frac{\pi}{4}\right)du$ in which $\sec(v) = 1/\cos(v)$. Consequently, the integral in (17) is rewritten as:

$$\mathcal{I}_{U_1}(x) = \frac{\pi}{4}\int_{-1}^{1}\mathcal{F}_{U_1}\left(\tan\left((u+1)\frac{\pi}{4}\right),x\right)\sec^2\left((u+1)\frac{\pi}{4}\right)du. \tag{18}$$

To approximate this standard integral using Chebyshev nodes of the first kind, we conceptually multiply and divide the integrand by the fundamental Chebyshev weight function $\sqrt{1-u^2}$. By absorbing the mapping Jacobian into the discrete weights, (18) can be tightly approximated by a finite sum according to the principles of GCQ:

$$\mathcal{I}_{U_1}(x) \approx \sum_{n=1}^{N}\omega_n\mathcal{F}_{U_1}(\chi_n,x), \tag{19}$$

where N defines a complexity-accuracy trade-off parameter. The transformed evaluation node χ_n is given by:

$$\chi_n = \tan\left((\psi_n+1)\frac{\pi}{4}\right), \tag{20}$$

with $\psi_n = \cos\left(\frac{(2n-1)\pi}{2N}\right)$ being the roots of the first-kind Chebyshev polynomial. Furthermore, the composite weight parameter ω_n, which absorbs the transformation Jacobian, is mathematically defined as:

$$\omega_n = \frac{\pi^2}{4N}\sqrt{1-\psi_n^2}\sec^2\left((\psi_n+1)\frac{\pi}{4}\right). \tag{21}$$

By substituting (19) back into (12), the final, computationally efficient closed-form expression for the effective capacity of the near user U_1 is obtained.

Applying a similar methodology for the far user U_2, the integral expectation $\mathcal{I}_{U_2}(y)$ defined in (15) is evaluated as:

$$\mathcal{I}_{U_2}(y) \approx \sum_{n=1}^{N}\omega_n\mathcal{F}_{U_2}(\chi_n,y), \tag{22}$$

where the composite core function $\mathcal{F}_{U_2}(z,y)$ is formulated as:

$$\mathcal{F}_{U_2}(z,y) = \left(1+\frac{a_2\bar{\gamma}zy}{a_1\bar{\gamma}zy+1}\right)^{-Q}\frac{2}{\Omega_2}K_0\left(2\sqrt{\frac{z}{\Omega_2}}\right). \tag{23}$$

Ultimately, the comprehensive EC for the far user is achieved by substituting (22) evaluated at both possible state parameters μ_2 and ν_2 into (14). In the subsequent numerical evaluations, all analytical curves represent the GCQ formulation evaluated with $N = 200$ quadrature nodes, while discrete markers represent empirical Monte Carlo simulations averaged over $N_{\mathrm{mc}} = 10^6$ independent channel realizations.

3.5 Asymptotic Performance Analysis

To gain deeper physical insights into the system performance at extreme operational regimes, we carry out asymptotic analyses for the effective capacity at the high-SNR and low-SNR regions.

3.5.1 High-SNR Regime ($\bar{\gamma} \to \infty$)

At strictly high transmit power, the system performance becomes interference-limited. By dividing both the numerator and the denominator of the SINR expressions in (7) and (8) by $\bar{\gamma} Z_i \tau_i^2$ and taking the limit as $\bar{\gamma} \to \infty$, the asymptotic SINRs converge to deterministic constants:

$$\Gamma_{U_1}^{\infty} = \lim_{\bar{\gamma}\to\infty} \frac{a_1}{\kappa a_2 + \frac{1}{\bar{\gamma} Z_1 \tau_1^2}} = \frac{a_1}{\kappa a_2}, \tag{24}$$

$$\Gamma_{U_2}^{\infty} = \lim_{\bar{\gamma}\to\infty} \frac{a_2}{a_1 + \frac{1}{\bar{\gamma} Z_2 \tau_2^2}} = \frac{a_2}{a_1}. \tag{25}$$

Substituting these deterministic limits into the effective capacity definition in (9), the high-SNR capacity ceilings for U_1 and U_2 are derived as:

$$R_{U_1}^{\infty} = \log_2 \left(1 + \frac{a_1}{\kappa a_2}\right), \tag{26}$$

$$R_{U_2}^{\infty} = \log_2 \left(1 + \frac{a_2}{a_1}\right). \tag{27}$$

Remark 2: Equation (26) reveals a critical insight: in the high-SNR regime, the effective capacity of the near user U_1 is bounded by an error floor dictated solely by the power allocation factors and the imperfect SIC severity (κ). Remarkably, this capacity ceiling is entirely independent of the fading channel properties (Ω_i), the phase misalignment statistics (τ_i) and the strictness of the delay constraint (Q). A similar behavior is observed for U_2 in (27).

3.5.2 Low-SNR Regime ($\bar{\gamma} \to 0$)

In the power-limited regime (i.e., $\bar{\gamma} \to 0$), the received SINR approaches zero ($\Gamma_i \to 0$). By applying the first-order Taylor series expansion $(1+x)^{-Q} \approx 1 - Qx$ for small x, the fundamental expectation in (9) can be tightly approximated as:

$$\mathbb{E}\{(1+\Gamma_i)^{-Q}\} \approx 1 - Q\mathbb{E}\{\Gamma_i\}. \tag{28}$$

Furthermore, by converting the base-2 logarithm in (9) to the natural logarithm via the change-of-base identity $\log_2(x) = \frac{\ln(x)}{\ln 2}$ and utilizing the natural logarithm approximation $\ln(1-v) \approx -v$ for $v \to 0$, the effective capacity is asymptotically linearized with respect to the expected SINR:

$$R_i^{\text{low}} \approx -\frac{1}{Q}\frac{\ln(1 - Q\mathbb{E}\{\Gamma_i\})}{\ln 2} \approx \frac{\mathbb{E}\{\Gamma_i\}}{\ln 2}. \tag{29}$$

For the near user U_1, when $\bar{\gamma} \to 0$, the interference term in the denominator of (7) becomes negligible, yielding $\Gamma_{U_1} \approx a_1 \bar{\gamma} Z_1 \tau_1^2$. Exploiting the statistical independence between the cascaded channel Z_1 and the alignment amplitude τ_1, the low-SNR slope for U_1 is derived as:

$$R_{U_1}^{\text{low}} = \frac{a_1 \bar{\gamma} \Omega_1 (\text{erf}(\rho_1)\mu_1 + [1 - \text{erf}(\rho_1)]v_1)}{\ln 2}. \tag{30}$$

Following a similar mathematical procedure, the asymptotic capacity slope for the far user U_2 is formulated as:

$$R_{U_2}^{\text{low}} = \frac{a_2 \bar{\gamma} \Omega_2 (\text{erf}(\rho_2)\mu_2 + [1 - \text{erf}(\rho_2)]v_2)}{\ln 2}. \tag{31}$$

Unlike the high-SNR ceiling, (30) and (31) demonstrate that the low-SNR capacity is highly sensitive to the phase misalignment statistics and the average channel conditions, growing linearly with the transmit SNR in the linear scale.

4. NUMERICAL RESULTS

This section validates the derived analytical and asymptotic formulations through Monte Carlo simulations. Unless stated otherwise, all analytical curves depicted in the figures correspond to the GCQ analytical framework evaluated at $N = 200$ nodes, whereas discrete markers denote Monte Carlo simulation averages over $N_{\mathrm{mc}} = 10^6$ independent channel realizations. For the convergence benchmark in Fig. 6, the 10^6-realization Monte Carlo baseline exhibits a measured 95% confidence error band of ±0.0031 bits/s/Hz (SE $\approx 1.57 \times 10^{-3}$ bits/s/Hz), providing a stable reference line for evaluating quadrature truncation accuracy. For simplicity, the default simulation parameters are configured as: $a_1 = 0.2, a_2 = 0.8, \kappa = 0.01, \mu_i = 0.8, v_i = 0.2, \Theta_i = \pi/90, B = 2, T = 6.5, \Omega_{SR} = 0.5, \Omega_{RU_1} = 1$ and $\Omega_{RU_2} = 0.75$. These channel gain settings $(\Omega_{RU_1} > \Omega_{RU_2})$ explicitly reflect the asymmetric spatial distribution of the two NOMA users, where the near user U_1 enjoys lower path attenuation from the ARR compared to the far user U_2 [13]. In addition, the Gauss-Chebyshev parameter is selected as $N = 200$ to maintain a measured relative truncation error on the order of 10^{-4}.

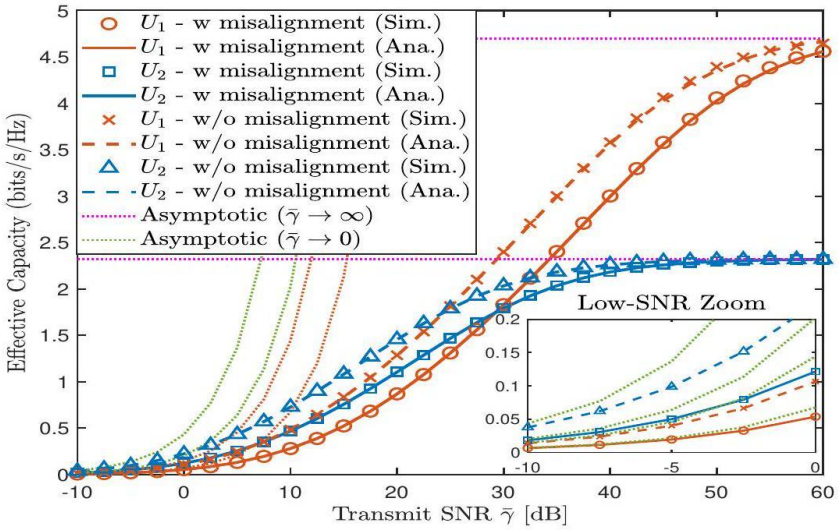


Figure 2. Effective capacity *versus* transmit SNR.

Fig. 2 plots the EC of both users *versus* the transmit SNR $\bar{\gamma}$, configured with a delay QoS exponent of $\vartheta = 0.1$, to evaluate the impact of phase misalignment on system performance. It is clear that the analytical results are in perfect agreement with the Monte Carlo simulation ones across the entire considered SNR range, thereby validating the accuracy of our mathematical derivations, while the theoretically derived asymptotic curves accurately predict the system's behavior in both the low-SNR and high-SNR regimes. The figure explicitly reveals that when the system operates under ideal conditions without phase misalignment (w/o misalignment), the EC of both users improves significantly compared to the practical scenario with phase errors (w misalignment), emphasizing the detrimental impact of imperfect beam steering on the overall transmission rate. Comparing the two users, in the low-to-moderate SNR region (from -10 dB to approximately 25 dB), the far user (U_2) achieves a better EC performance than the near user (U_1) owing to the NOMA power allocation strategy that inherently assigns a larger power coefficient to U_2 to guarantee user fairness. Conversely, when the transmit SNR exceeds the 20 dB threshold, the EC of U_1 grows rapidly and strictly outperforms that of U_2. Finally, it is noteworthy that as the SNR further increases, the ECs of both users eventually converge to constant asymptotic ceilings; this saturation occurs, because both users inherently suffer from interference when decoding their own information, which specifically arises from imperfect SIC for U_1 and the non-orthogonal signal mixture for U_2, indicating that arbitrarily increasing the transmit power beyond a certain level does not lead to higher ECs.

Fig. 3 plots the EC of both users versus the delay QoS exponent ϑ under transmit SNRs of $\bar{\gamma} = 10$ dB and $\bar{\gamma} = 20$ dB. As expected, an increase in ϑ implies a stricter delay constraint, causing the EC of all configurations to decrease monotonically and gradually flatten out as ϑ approaches 1. Observing the user behaviors, U_2 generally achieves a better EC than U_1 at $\bar{\gamma} = 10$ dB due to the larger power allocation factor of NOMA, while increasing the SNR to $\bar{\gamma} = 20$ dB yields a massive performance boost,

significantly elevating the capacities of both users, especially U_1. Finally, comparing the two alignment conditions clearly reveals the detrimental impact of phase errors, since the ideal scenario (w/o misalignment) consistently and strictly outperforms the practical case (w misalignment) across the entire range of ϑ for both users, thereby highlighting the critical importance of accurate phase synchronization in ensuring reliable, low-latency communications.

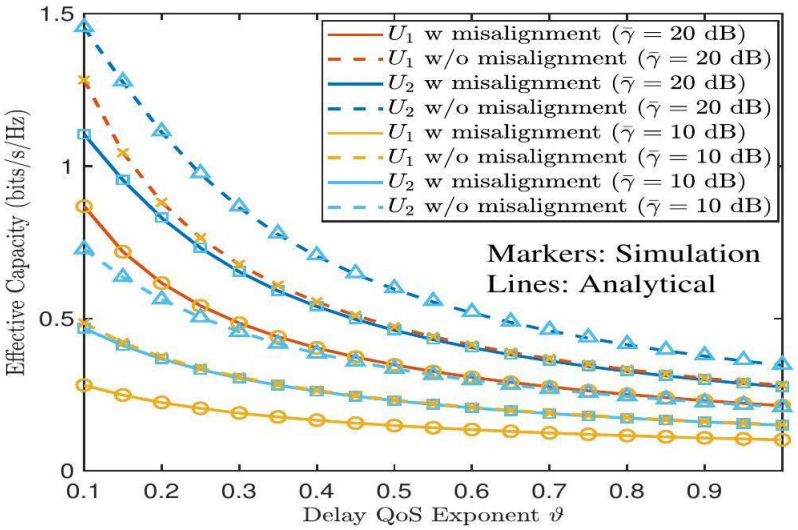


Figure 3. Effective capacity *versus* the delay QoS exponent ϑ.

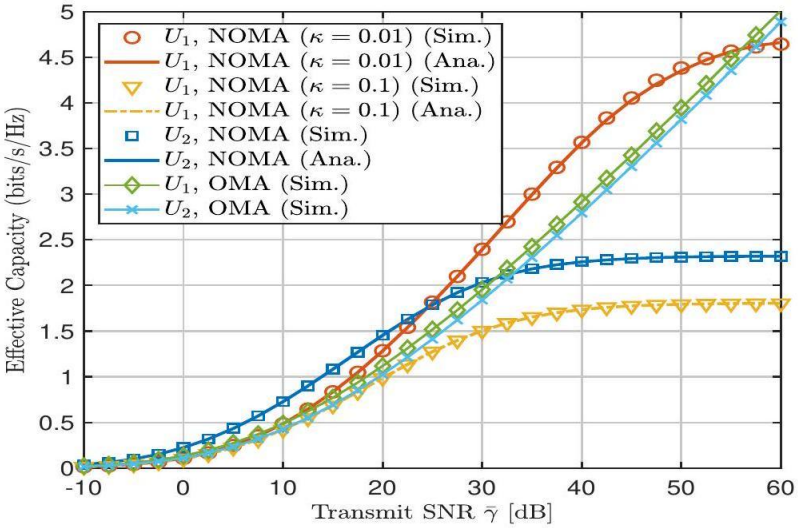


Figure 4. Comparison between NOMA and OMA for the effective capacity *versus* transmit SNR at two users.

Next, Fig. 4 compares the EC of NOMA and OMA systems *versus* the transmit SNR $\bar{\gamma}$ under varying levels of imperfect SIC ($\kappa = 0.01$ and $\kappa = 0.1$). To ensure a fair performance benchmark, the OMA scheme is configured using time-division orthogonal resource allocation where each user utilizes a fractional slot duration of $T/2$ with full transmit power P, resulting in a scaled delay parameter $Q_{\mathrm{OMA}} = Q/2$ and interference-free reception. In the low-to-medium SNR regime, NOMA exhibits a clear superiority over OMA; specifically, NOMA U_1 with a low residual interference ($\kappa = 0.01$) significantly outperforms its OMA counterpart until $\bar{\gamma}$ reaches approximately 55 dB, while NOMA U_2 surpasses OMA U_2 for SNRs below 32 dB. However, in the high-SNR region, the performance of NOMA users experiences saturation ceilings due to the inherent inter-user interference. Specifically, the EC of U_2 converges to a constant limit of around 2.3 bits/s/Hz and U_1 with a stronger imperfect SIC ($\kappa = 0.1$) ceilings early at approximately 1.8 bits/s/Hz. Conversely, since OMA completely eliminates inter-user interference through orthogonal resource allocation, the EC of both OMA users grows continuously with the transmit SNR without any error floors, eventually outperforming NOMA in the high-SNR regime.

Fig. 5 illustrates the EC of both users *versus* the transmit SNR $\bar{\gamma}$ to investigate the system's performance under varying main-lobe active gains (μ_i) and side-lobe leakage gains (v_i). While the EC of the far user U_2 is superior in the low-SNR regime, it rapidly hits a saturation ceiling due to inter-user interference, allowing the near user U_1 to overtake it and achieve significantly higher capacity at higher SNR levels. Furthermore, the inset clearly highlights the impact of the main-lobe and side-lobe gain configurations. Interestingly, the configuration with a lower main-lobe gain and higher side-lobe leakage ($\mu_i = 0.7$ and $v_i = 0.3$) consistently delivers the highest EC for both users, whereas the highly directive setup ($\mu_i = 0.9$ and $v_i = 0.1$) results in the lowest capacity. This ordering occurs, because under $\zeta_i = \sqrt{\Theta_i/10}$, the side-lobe leakage probability ($P_{\text{mis}} \approx 55.5\%$) exceeds the mainlobe alignment probability $\left(P_{\text{align}} \approx 44.5\%\right)$. Consequently, increasing the side-lobe gain v_i improves the average effective beam gain $\mathbb{E}[\tau_i^2] = P_{\text{align}}\,\mu_i + P_{\text{mis}}\,v_i$ more significantly than increasing the main-lobe gain μ_i (yielding $\mathbb{E}[\tau_i^2] = 0.4780$ for $\mu_i = 0.7, v_i = 0.3$ versus 0.4562 for $\mu_i = 0.9, v_i = 0.1$). This demonstrates that variations in μ_i and v_i considerably influence the decoding conditions and overall throughput, highlighting the necessity of carefully tuning these antenna parameters to optimize system performance under practical alignment imperfections.

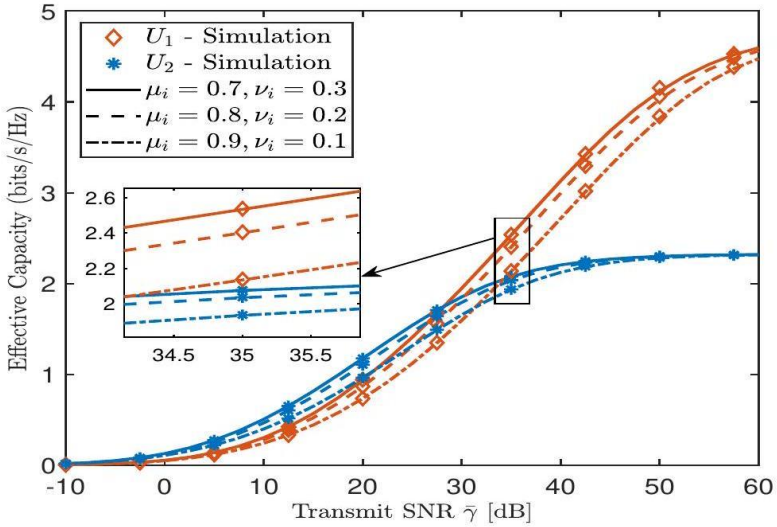


Figure 5. Effective capacity *versus* transmit SNR$\bar{\gamma}$ for varying main-lobe active gains (μ_i) and side-lobe leakage gains (v_i).

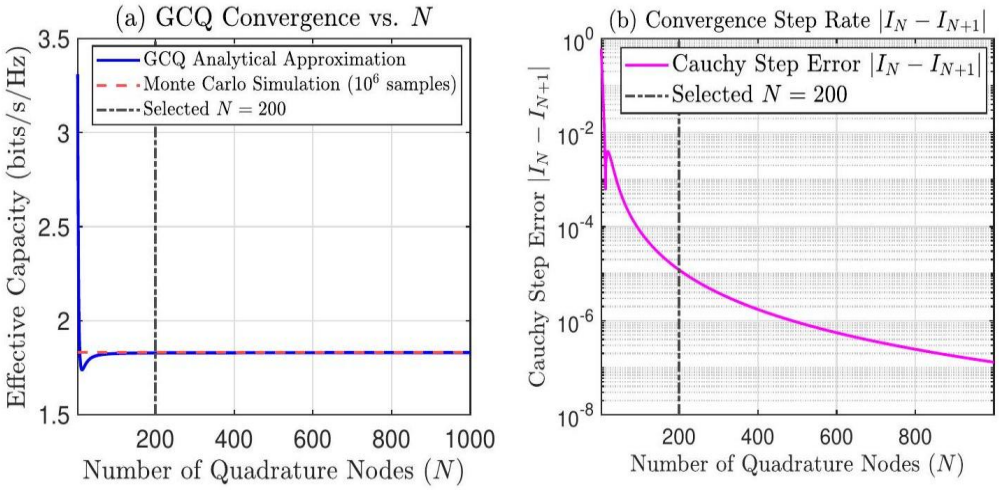


Figure 6. (a) Convergence trajectory of the GCQ analytical EC evaluation *versus* quadrature nodes $N \in [2, 1000]$ and (b) Cauchy step error rate $|I_N - I_{N+1}|$ for U_1 at $\bar{\gamma} = 30$ dB, $a_1 = 0.2, a_2 = 0.8, \kappa = 0.01$, $\mu_1 = 0.8$ and $v_1 = 0.2$.

To evaluate the convergence of the GCQ analytical framework and justify the selection of $N = 200$, Fig. 6 plots the EC evaluation *versus* node density $N \in [2,1000]$ for user U_1 at $\bar{\gamma} = 30$ dB. Specifically, Fig. 6(a) demonstrates that while lower node orders $(N < 30)$ exhibit approximation deviations (e.g.,

$I_{30} = 1.7906$ bits/s/Hz), the GCQ evaluation steadily approaches the high-order benchmark as N increases ($I_{200} = 1.8287, I_{500} = 1.8298$ and $I_{1000} = 1.8299$ bits/s/Hz). Additionally, Fig. 6(b) presents the Cauchy step error rate $|I_N - I_{N+1}|$, showing stepwise numerical stabilization. Relative to I_{1000}, setting $N = 200$ achieves a measured absolute truncation error of 1.27×10^{-3} bits $/s/$Hz, corresponding to a relative truncation error of $6.94 \times 10^{-4} (\approx 0.069\%)$. This error level on the order of 10^{-4} confirms that $N = 200$ balances mathematical precision and computational complexity.

To evaluate the practical resilience of the proposed ARR-assisted NOMA framework under channel state uncertainty, we incorporate a channel estimation error model where the true channel gain is $g = \hat{g} + e$, with $e \sim \mathcal{CN}(0, \sigma_e^2)$ representing complex Gaussian estimation error. Taking both imperfect SIC (κ) and channel estimation error (σ_e^2) into account, the effective SINR for user i incorporates a power-scaling residual noise floor of $\sigma_e^2 \bar{\gamma} \tau_i^2$ in its denominator. Fig. 7 illustrates the effective capacity of both U_1 and U_2 *versus* transmit SNR $\bar{\gamma}$ across varying channel estimation error variances $\sigma_e^2 \in \{0, 0.01, 0.05, 0.10\}$. As expected, the ideal Perfect CSI scenario ($\sigma_e^2 = 0$) provides the upper-bound baseline, allowing U_1 to achieve superior throughput over U_2 due to successful SIC decoding. However, when channel estimation errors are present ($\sigma_e^2 > 0$), the power-scaling residual estimation noise term ($\sigma_e^2 \bar{\gamma}$) severely degrades user throughput and forces both users into early capacity saturation ceilings at high SNR regimes ($\bar{\gamma} \geq 30$ dB). Crucially, as highlighted in the inset zoom, U_1 experiences a more pronounced capacity degradation than U_2 under ipCSI; this occurs, because U_1 receives a smaller power allocation ($a_1 = 0.2$), making its signal more vulnerable to the channel estimation noise floor compared to $U_2 (a_2 = 0.8)$. Nevertheless, under mild estimation error conditions ($\sigma_e^2 = 0.01$), the system preserves substantial throughput (achieving over 1.45 bits/s/Hz for U_2 and 1.30 bits/s/Hz for U_1), thereby demonstrating the inherent robustness and practical viability of our proposed network framework in realistic wireless environments.

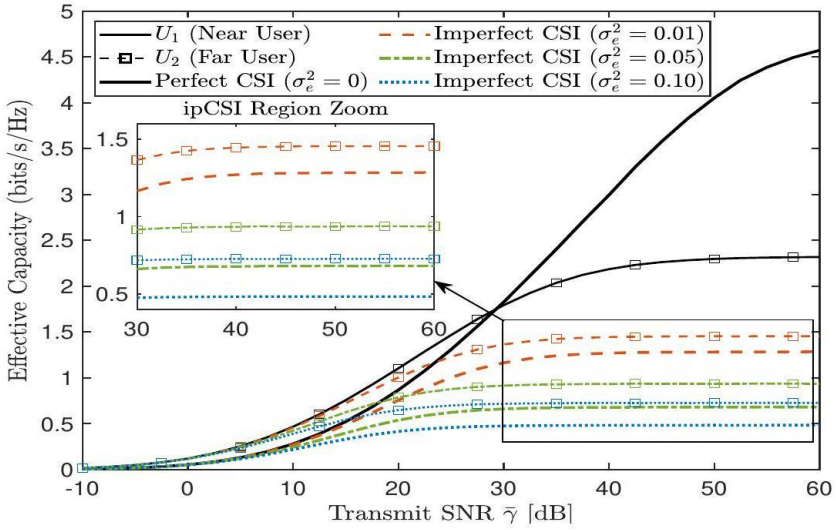


Figure 7. Effective capacity of U_1 and U_2 *versus* transmit SNR $\bar{\gamma}$ under perfect CSI($\sigma_e^2 = 0$) and imperfect CSI($\sigma_e^2 \in \{0.01, 0.05, 0.10\}$) with $a_1 = 0.2, a_2 = 0.8, \kappa = 0.01, \mu_i = 0.8$ and $v_i = 0.2$.

Fig. 8 illustrates the impact of imperfect SIC ($\kappa \in \{0.001, 0.01, 0.05, 0.1, 0.2, 0.5, 1.0\}$) on U_1 's effective capacity over transmit SNRs up to $\bar{\gamma} = 80$ dB, benchmarked against U_2. At low SNR ($\bar{\gamma} \leq 0$ dB), background noise dominates, resulting in low throughput across all configurations. As transmit power increases ($\bar{\gamma} > 20$ dB), residual interference under imperfect SIC ($\kappa a_2 \bar{\gamma} X_1 \tau_1^2$) becomes dominant, causing U_1 's capacity curves to saturate toward the asymptotic limits predicted by (26), $R_{U_1}^{\infty} = \log_2 \left(1 + \frac{a_1}{\kappa a_2}\right)$. Extending the evaluation range to 80 dB confirms that for $\kappa = 0.001$, U_1 's throughput approaches its theoretical ceiling of 7.97 bits/s/Hz (reaching 7.94 bits/s/Hz at 80 dB). For larger κ values (0.01 to 1.0), the numerical capacity ceilings match their theoretical bounds at 4.70, 2.58, 1.81, 1.17, 0.58 and 0.32 bits/s/Hz, respectively. Notably, when $\kappa \geq 0.1$, U_1 's saturated throughput falls below U_2's 's baseline (≈ 2.32 bits/s/Hz), indicating that maintaining $\kappa \leq 0.05$ is required for U_1 to preserve its NOMA performance advantage over U_2.

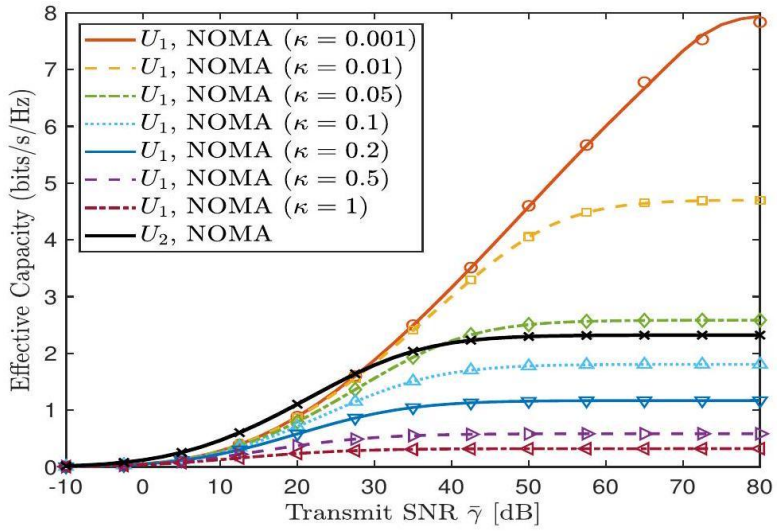
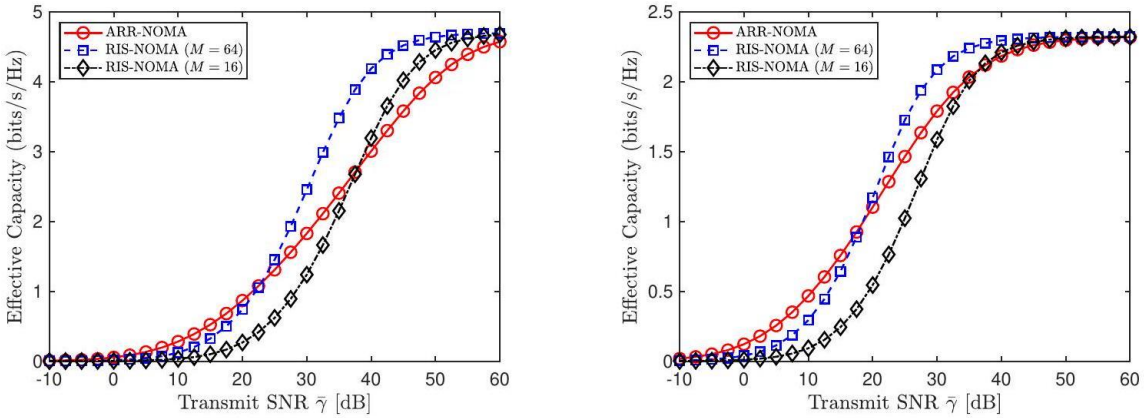


Figure 8. Effective capacity of U_1 *versus* transmit SNR $\bar{\gamma}$ under varying imperfect SIC parameters $\kappa \in \{0.001, 0.01, 0.05, 0.1, 0.2, 0.5, 1.0\}$, compared with the U_2 baseline ($a_1 = 0.2, a_2 = 0.8$).



(a) Near User U_1 (b) Far User U_2

Figure 9. Effective capacity comparison between proposed ARR-NOMA and passive RIS-NOMA ($M \in \{16, 64\}$): (a) Near user U_1, (b) Far user U_2.

To quantitatively demonstrate the performance advantage of active repeaters over passive reflection surfaces across all network nodes, Fig. 9(a) and Fig. 9(b) present direct Monte Carlo simulation comparisons of effective capacity for user U_1 (near user) and user U_2 (far user), respectively. As observed in both sub-figures, the proposed ARR-NOMA framework achieves superior effective capacity over passive RIS-NOMA ($M \in \{16, 64\}$) in the low-to-medium SNR regime ($\bar{\gamma} \leq 20$ dB); this highlights the crucial benefit of active amplification in overcoming severe double path-loss attenuation when transmit power is limited. However, as the transmit SNR increases into the medium-to-high power regime (20 dB $< \bar{\gamma} < 50$ dB), passive RIS-NOMA with $M = 64$ elements surpasses ARR-NOMA, leveraging its large passive beamforming array gain ($\propto M^2$) without suffering from amplifier noise limitations. Finally, at very high SNRs ($\bar{\gamma} \geq 50$ dB), throughput curves for all architectures approach capacity ceilings dictated by residual interference ($\kappa = 0.01$ for U_1 and $a_1 = 0.2$ for U_2). These findings confirm that active ARR-NOMA is particularly well-suited for power-limited and low-SNR coverage extension scenarios in B5G/6G networks.

Finally, Fig. 10 illustrates the fundamental capacity trade-off between the near user (U_1) and the far user (U_2) in the proposed NOMA system under varying delay constraints. It is clearly observed that as the power allocation factor a_2 increases, more transmit power is prioritized for the far user, which steadily enhances the effective capacity of U_2, but comes at the severe expense of U_1 's performance. Furthermore, the figure distinctly highlights the critical impact of the delay QoS exponent ϑ; specifically, as ϑ increases from 0.1 to 0.5, the stricter delay constraints impose a heavier penalty on the system, leading to a significant and uniform degradation in the achievable effective capacity for both

users across the entire power allocation spectrum. This downward shift in the capacity curves confirms the theoretical expectation that supporting highly delay-sensitive communications inherently requires a sacrifice in the maximum maintainable data rates.

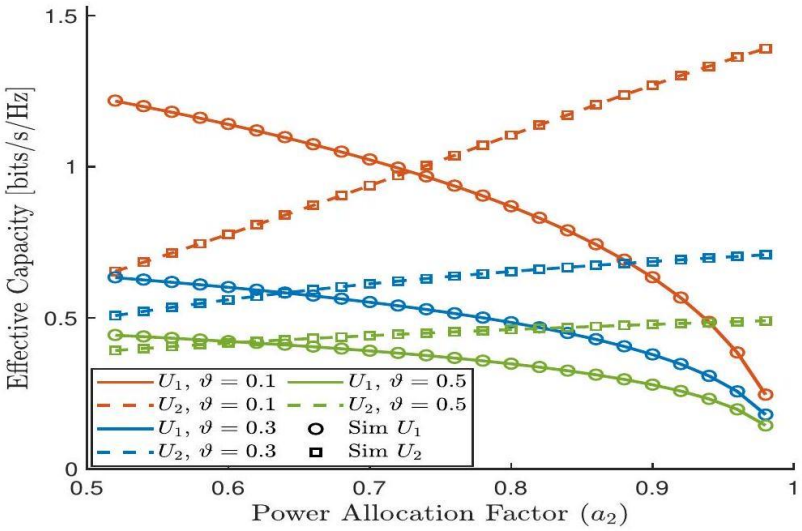


Figure 10. Effective capacity *versus* power allocation factor (a_2), with $\bar{\gamma} = 20$ dB.

5. CONCLUSION

In this paper, we have provided a detailed study of the effective capacity of a downlink ARR-assisted NOMA communication system under severe delay constraints. The detrimental effects of phase misalignment error at the sectorized repeater antenna as well as the imperfect SIC at the near user were explicitly incorporated in the analytical model. Employing the Gauss-Chebyshev quadrature method, we have obtained computationally efficient approximations of the effective capacity of both users, the accuracies of which were rigorously validated *via* Monte Carlo simulations. Through detailed asymptotic analysis, we demonstrated that the effective capacities experience saturation ceilings in the high-SNR regime due to inherent inter-user and residual interference, whereas they scale linearly in the low-SNR power-limited region. The numerical findings highlighted a fundamental capacity trade-off between the near and far users, which is heavily governed by the power allocation strategy and the strictness of the delay constraint. Furthermore, it was shown that accurate beam alignment is crucial, as phase errors heavily penalize the achievable data rates. Moreover, the ARR-assisted NOMA system was shown to outperform its OMA counterpart at low-to-medium transmit powers, though OMA regains the advantage at very high SNRs due to the absence of interference ceilings. Future research directions may include extending this analytical framework to multi-antenna configurations, exploring other advanced multiple access schemes, such as rate-splitting multiple access (RSMA) or investigating the system resilience under imperfect channel state information conditions.

REFERENCES

[1] M. U. A. Siddiqui et al., "URLLC in Beyond 5G and 6G Networks: An Interference Management Perspective," IEEE Access, vol. 11, pp. 54639-54663, 2023.

[2] Y. Liu, Y. Deng, A. Nallanathan and J. Yuan, "Machine Learning for 6G Enhanced Ultra-reliable and Low-latency Services," IEEE Wireless Communications, vol. 30, no. 2, pp. 48-54, 2023.

[3] A. Pourkabirian et al., "A Vision of 6G URLLC: Physical-layer Technologies and Enablers," IEEE Communications Standards Magazine, vol. 8, no. 2, pp. 20-27, 2024.

[4] C. -B. Le and T. P. Tran, "Analytical Insights into the Average Block Error rate of Fluid Antenna Systems under Short-packet Constraints," Jordanian Journal of Computers and Information Technology (JJCIT), vol. 12, no. 3, pp. 283-296, 2026.

[5] S. Sobhi-Givi et al., "Efficient Optimization in RIS-assisted UAV System Using Deep Reinforcement Learning for mmWave-NOMA 6G Communications," IEEE Internet of Things Journal, vol. 12, no. 14, pp. 26042-26057, 2025.

[6] M. Ahmed et al., "Efficient Resource Management for NOMA-enabled UAV Communications in 6G IRS-Assisted Vehicular Networks," IEEE Transactions on Intelligent Transportation Systems, vol. 27, no. 2, pp. 2706-2715, 2026.

[7] F. Chai, Q. Zhang, H. Yao, X. Xin, R. Gao, D. Wu and F. R. Yu, "A Hybrid NOMA-OMA Framework for Multi-user Offloading in Mobile Edge Computing System," IEEE Transactions on Services Computing, vol. 18, no. 4, pp. 1881-1892, 2025.

[8] B. E. Y. Belmekki and M.-S. Alouini, "NOMA as the Next-Generation Multiple Access in Non-terrestrial Networks," Proceedings of the IEEE, vol. 112, no. 9, pp. 1303-1345, 2024.

[9] M. M. Salim et al., "Cooperative NOMA Meets Emerging Technologies: A Survey for Next-Generation Wireless Networks," IEEE Open J. of the Comm. Society, vol. 6, pp. 9247-9286, 2025.

[10] S. P. Indraganti et al., "Survey of Cooperative NOMA for Beyond 5G: State-of-the-Art, Applications and Research Directions," IEEE Open J. of the Comm. Society, vol. 7, pp. 40-94, 2026.

[11] M. Zhou, J. Sang, B. Gao, W. Tang, X. Li, S. Jin and E. Basar, "A Floating-Intercept Path Loss Model Considering RIS Array Gain in Practical Environments," IEEE Transactions on Communications, vol. 73, no. 12, pp. 13935-13952, 2025.

[12] A. -T. Le, T. -H. Vu, N. H. Tu, T. N. Nguyen, L. -T. Tu and M. Voznak, "Active-Reconfigurable-Repeater-assisted NOMA Networks in Internet of Things: Reliability, Security and Covertness," IEEE Internet of Things Journal, vol. 12, no. 7, pp. 8759-8772, 2025.

[13] T. -H. Vu and M. Le-Tran, "Reconfigurable Repeater-aided NOMA Systems under Imperfect SIC and Phase Misalignment Error," Digital Signal Processing, vol. 183, pp. 106380, 2026.

[14] T. -H. Vu, N. H. Tu and V. N. Q. Bao, "Study on Reconfigurable Repeater-based RSMA Systems," IEEE Wireless Communications Letters, vol. 14, no. 5, pp. 1371-1375, 2025.

[15] H. Iimori, E. Kurihara, T. Yoshida, J. Vieira and S. Malomsoky, "Amplification Strategy in Repeater-Assisted MIMO Systems via Minorization Maximization," Proc. of the GLOBECOM 2023-2023 IEEE Global Communications Conf., pp. 4989-4994, Kuala Lumpur, Malaysia, 2023.

[16] B. T. Walkenhorst and M. A. Ingram, "Repeater-assisted Capacity Enhancement (RACE) for MIMO Links in a Line-of-Sight Environment," Proc. of the 2009 IEEE Int. Conf. on Communications, pp. 1-6, Dresden, Germany, 2009.

[17] A. -T. Le et al., "Power Beacon and NOMA-assisted Cooperative IoT Networks with Co-channel Interference: Performance Analysis and Deep Learning Evaluation," IEEE Transactions on Mobile Computing, vol. 23, no. 6, pp. 7270-7283, 2024.

[18] M. Liu, J. Fang, Y. Liu, D. Niyato, C. Masouros and F. Wang, "SIC Ordering for Impaired NOMA-ISAC Systems: A Universal Theoretical Framework," IEEE Transactions on Wireless Communications, vol. 25, pp. 13669-13684, 2026.

[19] X. Li, Y. Zheng, M. D. Alshehri, L. Hai, V. Balasubramanian, M. Zeng and G. Nie, "Cognitive AmBC-NOMA IoV-MTS Networks with IQI: Reliability and Security Analysis," IEEE Transactions on Intelligent Transportation Systems, vol. 24, no. 2, pp. 2596-2607, Feb. 2023.

[20] Y. Xu, W. Lv, H. Ni, Q. Chen, C. Huang and Z. Huang, "Performance Analysis of RIS-Aided NOMA-based Backscatter Communication with Imperfect CSI and SIC," IEEE Transactions on Vehicular Technology, pp. 1-12, 2026.

[21] L. Yuan, M. Mo, N. Yang and F. Fang, "Impacts of Imperfect CSI, Residual Hardware Impairments and Imperfect SIC on Alamouti-coded Short-Packet NOMA Systems with Hybrid Multicast-Unicast Transmission," IEEE Internet of Things Journal, vol. 12, no. 24, pp. 54468-54482, 2025.

[22] S. Eum, S. Arakawa and M. Murata, "Deterministic and Probabilistic Scheduling for Latency Guarantees in B5G/6G Network Management," IEEE Transactions on Network and Service Management, vol. 23, pp. 2149-2165, 2026.

[23] Z. Shi, T. A. Tsiftsis, W. Tan, G. Yang, S. Ma and M. -S. Alouini, "Effective Capacity for Renewal Service Processes with Applications to HARQ Systems," IEEE Transactions on Communications, vol. 67, no. 9, pp. 6556-6571, 2019.

[24] Z. Mohamed, M. Amjad, L. Musavian and S. Aïssa, "Effective Capacity of Non-orthogonal Multiple Access with Finite Block-length for Low-latency Communications," IEEE Transactions on Wireless Communications, vol. 24, no. 10, pp. 8267-8282, 2025.

[25] N.-H. Nguyen, M.-V. Nguyen, M.-X. Pham and S.-Q. Nguyen, "On the Reliability and Spectral Efficiency of Multi-antenna AF Relay-aided NOMA Networks," Jordanian Journal of Computers and Information Techno. (JJCIT), vol. 12, no. 2, pp. 212-229, DOI: 10.5455/jjcit.71-1772102720, Jun. 2026.

[26] H.-N. Nguyen and P.-C. Ngo, "On the Effect of Keyhole Channel in RSMA Networks: A Theoretical Outage Analysis," Jordanian Journal of Computers and Information Technology (JJCIT), vol. 12, no. 2, pp. 201-211, DOI: 10.5455/jjcit.71-1771168818, Jun. 2026.

[27] L.-D. Huynh, L.-T. Tu, Q.-S. Nguyen and T. N. Nguyen, "Ambient Backscatter-assisted Relaying in Symbiotic Radio Networks with Energy Harvesting: Performance Analysis," Jordanian Journal of Computers and Information Technology (JJCIT), vol. 12, no. 1, pp. 82-97, DOI: 10.5455/jjcit.71-1765426560, Mar. 2026.

[28] H.-N. Nguyen, S.-P. Le, Q.-S. Vu, Q.-S. Nguyen and E. Chromy, "Secure Performance Analysis of Satellite-terrestrial Networks-assisted Backscatter Device," Jordanian Journal of Computers and Information Techno. (JJCIT), vol. 11, no. 4, pp. 484-498, DOI: 10.5455/jjcit.71-1757510806, Dec. 2025.

[29] Q.-S. Nguyen, C.-H. Tran, T.-D. Tran, M. Tran and B.-S. Kim, "Securing Wireless Communications with Energy Harvesting and Multi-antenna Diversity," Jordanian Journal of Computers and Information Technology (JJCIT), vol. 11, no. 2, pp. 197-210, DOI: 10.5455/jjcit.71-1732244909, Jun. 2025.

[30] Q.-S. Nguyen, C.-H. Tran, N.-L. Nguyen, B.-V. Minh and L. Rejfek, "Power Beacon-assisted Energy Harvesting in D2D Network under Co-channel Interferences: Symbol Error Rate Analysis," Jordanian Journal of Computers and Information Technology (JJCIT), vol. 11, no. 4, pp. 517-532, DOI: 10.5455/jjcit.71-1755140290, Dec. 2025.

[31] A. Reda, T. Mekkawy and A. Mahran, "Towards Optimizing the Downlink Transmit Power in UAV-integrated IRS Wireless Systems," Jordanian Journal of Computers and Information Technology (JJCIT), vol. 11, no. 2, pp. 184-196, DOI: 10.5455/jjcit.71-1727208249, Jun. 2025.

[32] S. Ahuja, H. Chhabra and A. Jain, "Performance Enhancement of NOMA for Emerging Wireless Networks Using SIC Repeaters," Proc. of the 2024 2nd Int. Conf. on Emerging Trends in Information Technology and Engineering (ICETITE), pp. 1-7, Vellore, India, 2024.

[33] Y. Pei, X. Yue, W. Yi, Y. Liu, X. Li and Z. Ding, "Secrecy Outage Probability Analysis for Downlink RIS-NOMA Networks with On-Off Control," IEEE Transactions on Vehicular Technology, vol. 72, no. 9, pp. 11772-11786, 2023.

[34] D. -T. Vo, T. N. Nguyen, A. -T. Le, V. -D. Phan and M. Voznak, "Holographic Reconfigurable Intelligent Surface-aided Downlink NOMA IoT Networks in Short-packet Communication," IEEE Access, vol. 12, pp. 65266-65277, 2024.

[35] A. P. Chrysologou, A. -A. A. Boulogeorgos and N. D. Chatzidiamantis, "When THz-NOMA Meets Holographic Reconfigurable Intelligent Surfaces," IEEE Communications Letters, vol. 27, no. 9, pp. 2516-2520, 2023.

[36] D. Choi and J. H. Lee, "Outage Probability of Two-Way Full-Duplex Relaying with Imperfect Channel State Information," IEEE Communications Letters, vol. 18, no. 6, pp. 933-936, 2014.

[37] C. -B. Le, D. -T. Do, A. Silva, W. U. Khan, W. Khalid, H. Yu and N. D. Nguyen, "Joint Design of Improved Spectrum and Energy Efficiency with Backscatter NOMA for IoT," IEEE Access, vol. 10, pp. 7504-7519, 2022.

[38] K. Wang, Z. Ding and R. Schober, "Antenna Activation for NOMA Assisted Pinching-antenna Systems," IEEE Wireless Communications Letters, vol. 14, no. 5, pp. 1526-1530, 2025.

[39] A. -A. A. Boulogeorgos and A. Alexiou, "Performance Analysis of Reconfigurable Intelligent Surface-assisted Wireless Systems and Comparison with Relaying," IEEE Access, vol. 8, pp. 94463-94483, 2020.

[40] S. Ghafoor, M. H. Rehmani and A. Davy, Next Generation Wireless Terahertz Communication Networks, ISBN: 9780367770426, CRC Press, 2021.

[41] L. T. T. Huyen, B. A. Duc, X. N. Tran, B. C. Nguyen, L. T. Dung and T. M. Hoang, "BLER and BER Performance of RSMA in Multiantenna Systems Over Nakagami Fading Channels," IEEE Internet of Things Journal, vol. 13, no. 14, pp. 31335-31349, 2026.

[42] X. Li, H. Liu, G. Li, Y. Liu, M. Zeng and Z. Ding, "Effective Capacity Analysis of AmBC-NOMA Communication Systems," IEEE Transactions on Vehicular Technology, vol. 71, no. 10, pp. 11257-11261, 2022.

[43] D. Qiao, M. C. Gursoy and S. Velipasalar, "Analysis of Energy Efficiency in Fading Channels under QoS Constraints," Proc. of the IEEE GLOBECOM 2008-2008 IEEE Global Telecommunications Conference, pp. 1-5, New Orleans, USA, 2008.

[44] T. C. Hieu, N. L. Cuong, B. C. Nguyen and P. T. Hiep, "Full-duplex Protocol for Vehicle-to-vehicle NOMA Relay System over Double Rayleigh Fading," Telecommunication Systems, vol. 80, no. 3, pp. 337-347, 2022.

[45] M. Abramowitz, I. A. Stegun and J. E. Romain, Handbook of Mathematical Functions, with Formulas, Graphs and Mathematical Tables, American Institute of Physics, 1966.

"Effective Capacity of ARR-aided NOMA Networks under Phase Misalignment and Imperfect SIC", C.-B. Le and T. P. Tran.

ملخص البحث:

يتناول هذا البحث التّأثير المشترك لعمليات إلغاء التّداخل المتتالية غير المثالية وأخطاء الطّور على السّعة الفعالة لشبكات الوصول المتعدّد غير المتعامد المدعومة بمكرّرات إشارة نشطة قابلة لإعادة التّشكيل. وفي ظلّ قيود صارمة على التّأخير الزّمني، تمّ استخدام تقنية "غاوس-تشيبيشيف" لتحليل سلوك النّظام من اجل استنباط صيغ تقريبية دقيقة للسّعة الفعالة للميتخدمين القريبين والبعيدين عبر قنوات تتّسم بتلاشي "رايلي" المستتلّ.

علاوة على ذلك، أجري تحليل تقاربي مفصّل في نطاقات نسب الإشارة ألى الضوضاء العالية والمنخفضة لاستخلاص رؤى فيزيائية حول أداء النّظام.

وتشير النّتائج التّحليلية والعددية إلى وجود حدود جوهرية لأداء النّظام؛ ففي نطاق نسب الإشارة إلى الضّوضاء العالية، تصبح السّعة الفعالة لمستخدمي النّظام مقيّدة بحدود خطأ حتميّة تعتمد فقط على معاملات تخصيص القدرة والتّداخُل المتبقي، وهي مُستقلة تماماً عن خصائص القناة ومتطلّبات التّأخير. وفي المقابل، في نطاق نسب الإشارة إلى الضّوضاء المنخفضة (حيث تكون القدرة هي العامل المقيّد)، تتناسب السّعات الفعالة خطّياً مع نسبة الإشارة إلى الضّوضاء عند الإرسال. كذلك تُظهر النّتائج أنّ متطلّبات جودة الخدمة الصّارمة وأخطاء الطّور الكبيرة تؤدّي إلى تقييد معدّلات الإرسال بشكلٍ حاد.

ورغم ذلك، ومع وجود عيوب في الأجهزة والقناة، فإنّ بنية النّظام المقترحة الّتي تعتمد على مكرّرات إشارة نشطة قابلة لإعادة التّشكيل تتفوّق بشكلٍ ملحوظ على بنية الوصول المتعامد التّقليدية في نطاقات نِسب الإشارة إلى الضّوضاء المنخفضة والمتوسّطة.

This article is an open access article distributed under the terms and conditions of the Creative Commons Attribution (CC BY) license (http://creativecommons.org/licenses/by/4.0/).